Bayesian differential moment tensor inversion: theory and application to the North Korea nuclear tests

Zhe Jia, Zhongwen Zhan, Donald Helmberger †

Seismological Laboratory, California Institute of Technology, Pasadena, CA 91125, USA

† Deceased on August 13, 2020

Corresponding author. Zhe Jia (zjia@gps.caltech.edu)

SUMMARY

Moment tensors are key to seismic discrimination but often require accurate Green's functions for estimation. This limits the regions, frequency bands, and wave types in moment tensor inversions. In this study, we propose a differential moment tensor inversion (diffMT) method that uses relative measurements to remove the path effects shared by clustered events, thereby improving the accuracy of source parameters. Using results from regular inversions as a priori distribution, we apply Bayesian Markov Chain Monte Carlo to invert the body- and surface-wave amplitude ratios of an event pair for refined moment tensors of both events. Applications to three North Korea nuclear tests from 2013 to 2016 demonstrate that diffMT reduces the uncertainties substantially compared with the traditional waveform-based moment tensor inversion. Our results suggest high percentages of explosive components with similar double-couple components for the North Korea nuclear tests.

Key words: Earthquake source observations, Inverse theory, Earthquake monitoring and test-ban treaty verification

1 INTRODUCTION

Seismic moment tensor provides a point-source approximation of the radiation pattern and a measure of the event size. Different combinations of isotropic (ISO), double couple (DC), and compensated linear vector dipole (CLVD) components can manifest the first-order physics of different event types, such as natural earthquakes, collapses, landslides, and nuclear explosions, thus being used for their discrimination (Alvizuri and Tape, 2018, Ford *et al.*, 2009, Cesca *et al.*, 2017). Furthermore, double-couple focal mechanisms provide important insights on regional stress state (Hauksson, 1994, Hardebeck and Hauksson, 2001, Wang and Zhan, 2020b), plate interface morphology (Hayes *et al.*, 2009, Bazargani *et al.*, 2013, Zhan *et al.*, 2012) and slab dynamics (Yang *et al.*, 2017, Liu *et al.*, 2021). In the past few decades, moment tensor inversion has gradually progressed from polarity-based to waveform-based inversion (Ekström *et al.*, 2012, Kanamori and Rivera, 2008, Zhu and Helmberger, 1996). At the theoretical level, Tape and Tape (2012, 2013, 2015) proposed a mathematically intuitive way to view the moment tensors and examine the explosive and tensile mechanisms. Zhu and Ben-Zion (2013) developed a parameterization of full moment tensors with well-defined parameters for source inversion. These progresses in theory and inversion, together with the improving Earth structural modeling, reduce the focal mechanism errors to about 20 degrees for most moderate to large events in the centroid moment tensor catalogs (Duputel *et al.*, 2012).

However, accurate full moment tensor inversions for shallow sources are still challenging. Robust moment tensor solutions are usually only retrievable at long periods (e.g. T>20s, (Minson and Dreger, 2008)) that are insensitive to small-scale structural heterogeneities. However, earthquakes and explosions of small to moderate size usually have limited near-field coverage and weak signals at long periods. For the short-period waves, modeling them is difficult because existing 3D crustal velocity models are often inadequate in capturing small scale heterogeneities at regional distances. Using inaccurate earth structural models could introduce errors in focal mechanisms and non-DC proportions (Frohlich and Davis, 1999). Taking the North Korea nuclear explosions as an example, different studies show nontrivial differences of moment tensor solutions (Cesca *et al.*, 2017, Chiang *et al.*, 2018, Alvizuri and Tape, 2018). For better azimuthal and take-off angle coverage, approaches that jointly invert regional and teleseismic waves have been proposed (Ni *et al.*, 2010, Ford *et al.*, 2012), but they still encounter difficulties from inaccurate Green's functions.

To accurately determine the moment tensors when the path structure is complex, approaches using 3D Green's functions have been introduced (Covellone and Savage, 2012, Wang and Zhan, 2020a). Most models used to calculate the 3D Green's function are travel-time- and waveform- based tomographic models. Travel time tomographic models, such as the LLNL model by Simmons et al. (2012) and the SALSA3D model by Ballard et al. (2016), can predict body waves arrivals with significantly reduced errors than 1D models, thereby being used to precisely detect and locate small seismic events. However, they are usually restricted by the smoothing in the inversions, and may not accurately fit the seismic waveforms. On the other hand, waveform-based tomographic models are more promising in explaining wiggles on seismograms (Tape *et al.*, 2009, Fichtner *et al.*, 2009, Bozdağ *et al.*, 2016). But most global and continental scale models use long-period waveforms (e.g. T>17s globally) for inversion, due to the high computational cost. Only for specific areas of dense seismic monitoring, adjoint tomographic inversions based on higher frequency seismic waveforms have been developed and implemented in source inversions (Savage *et al.*, 2014, Lee *et al.*, 2014, Jia *et al.*, 2020b).

To reduce the requirement of highly accurate velocity models, the empirical Green's function (EGF) methods are developed to study clustered explosions and earthquakes. Sites of artificial explosions are often clustered and share similar path and site effects. For example, all the North Korea nuclear tests were in the Punggye-ri site, within a few km from each other (Zhang and Wen, 2013, Zhang and Wen, 2015, Wang and Hutko, 2018, Xu *et al.*, 2020). As shown in Fig. 1, the regional waveforms from the Feb 2013 and Jan 2016 North Korea tests are highly similar at both broadband and long periods (T>5s), suggesting overlapping paths and common station terms. This similarity makes nuclear tests ideal for EGF methods, which removes the structural terms using relative measurements. Ni et al. (2010) used tectonic earthquakes to calibrate the path and site effects, thereby improving the moment tensor inversions of nuclear tests. Lay et al. (1984) inter-correlated source time functions and waveforms of two nuclear events to remove path influences and determine their yield and depths, and the method has also been applied on the North Korean nuclear explosions (Voytan *et al.*, 2019). For tectonic earthquakes, smaller EGF events can help investigate the mechanisms and ruptures of mainshocks, including the 1994 Northridge earthquake (Dreger, 1994) and the 2004 Sumatra earthquake (Vallée, 2007).

Among the EGF approaches, relative moment tensor inversion methods stand out as a particular category. Similar to the double-difference relocation algorithm which removes common travel time anomalies for more precise locations (Waldhauser and Ellsworth, 2000), relative moment tensor inversions eliminate the path and site amplifications to reduce moment tensor errors. Plourde and

Bostock (2019) used relative amplitudes of body waves among a cluster of seismic events to improve focal mechanisms. EGF methods greatly reduce moment tensor errors, but they can also introduce bias by assuming the reference event is well resolved. Dahm (1996) avoided the assumption on a single reference event by using arbitrary a priori constraint, but facing the issues of interference bias and lack of uncertainty assessments. To better assess errors and to avoid arbitrary selection of reference events, we need to incorporate Bayesian statistics to the relative moment tensor inversion methods with appropriate a priori information.

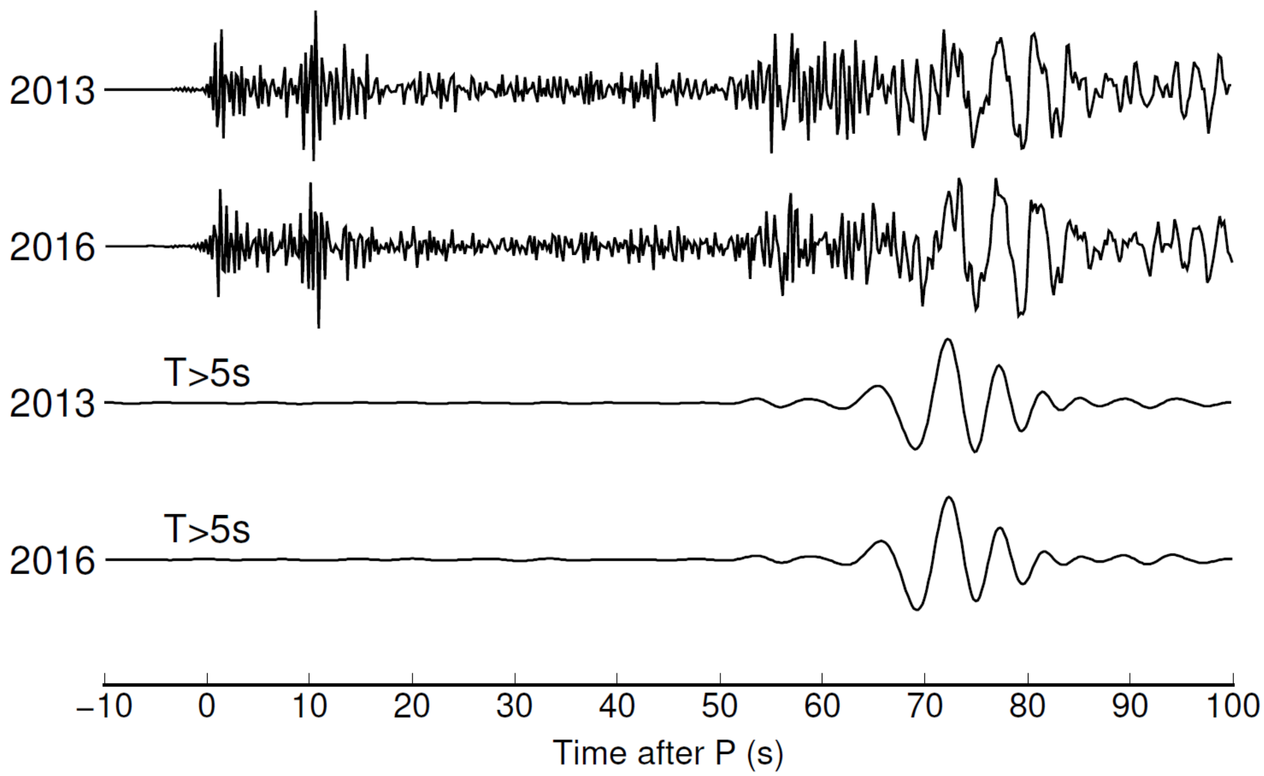

Figure 1. Waveform similarity of the Feb 2013 and Jan 2016 nuclear tests. The similarities in both broadband (top two) and low-passed filtered (bottom two) waveforms recorded at station MDJ suggest shared path/site effects. Note that P waves are only visible at short periods. The epicentral distance is about 400km.

In this study, we develop a differential moment tensor inversion (diffMT) algorithm to study paired seismic events in a Bayesian framework. We take amplitude ratios of various seismic phases to cancel out path and site effects, and expect reduced moment tensor errors. For nuclear tests, these should translate to better explosion discriminations and yield estimations. We verify the diffMT algorithm using synthetic data, and apply it to three North Korea nuclear tests between 2013 and 2016. We compare our results with traditional waveform inversion solutions, and analyze the explosion and tectonic release components of these tests.

2 METHODS

Our diffMT method refines the waveform-based moment tensor prior distribution with additional differential measurements for an event pair. There are two steps. First, we apply the generalized Cut-and-Paste (gCAP) inversion for moment tensor solutions and their uncertainties as the prior information. We then measure the amplitude ratios for regional and teleseismic P waves, regional Rayleigh and Love waves, and conduct Markov Chain Monte Carlo (MCMC) inversion on these differential measurements for the posterior distributions of moment tensor components.

2.1 Generalized Cut-and-Paste inversion for prior information

Our first step is equivalent to most traditional moment tensor inversions. In this study, we use gCAP (Zhu and Ben-Zion, 2013) as our main driver for the waveform inversion, as improved by Bai et al. (2020) to combine near-field and teleseismic data. The CAP methodology (Zhao and Helmberger, 1994, Zhu and Helmberger, 1996) breaks seismograms into Pnl and S/Surface waves, and models them simultaneously but allows different time shifts between observations and synthetics to accommodate inaccurate velocity models and earthquake locations. The generalized CAP (gCAP) method relieves the double couple restriction for full moment tensor inversions. Here, we search for six independent parameters, including moment magnitude (M_w), isotropic (ISO) and compensated linear vector dipole factor (CLVD) components (ζ and χ), strike, dip, and rake (Zhu and Ben-Zion, 2013). The proportion of isotropic (Λ^{ISO}), double couple (Λ^{DC}), and compensated linear vector dipole (Λ^{CLVD}) components are represented by

$$\Lambda^{ISO} = \zeta^2 \tag{1}$$

$$\Lambda^{DC} = (1-\zeta^2) * (1-\chi^2) \tag{2}$$

$$\Lambda^{CLVD} = (1-\zeta^2) * \chi^2. \tag{3}$$

We use the bootstrapping resampling approach (Zhan *et al.*, 2012, Jia *et al.*, 2017) to estimate the source parameter uncertainties, which is used as a priori constraint for the following Bayesian MCMC inversions. Calculations of Green's functions are based on the propagator matrix method with plane wave approximation (Kikuchi and Kanamori, 1991) for the teleseismic body waves, and the frequency-wavenumber integration method (Zhu and Rivera, 2002) for regional surface waves.

2.2 Prediction and measurement of amplitude ratios

We calculate amplitude ratios of regional Pn/P, teleseismic P, regional Rayleigh and Love waves from two events to cancel out the path and site effects. The far-field seismic waves of an event pair can be represented by

$$u_1(\boldsymbol{x},t) = M_{ij}^1 * G_{ij}(\boldsymbol{x},t) * S_1(t) * r(\boldsymbol{x}), \tag{4}$$

$$u_2(\boldsymbol{x},t) = M_{ij}^2 * G_{ij}(\boldsymbol{x},t) * S_2(t) * r(\boldsymbol{x}), \tag{5}$$

where M_{ij} is the full moment tensor, G_{ij} is the Green's function, S is the source time function, and r is the station amplification term. If we use body waves at periods longer than the source durations, we can reasonably approximate the studied events as point sources, and remove common path/site effects by taking amplitude ratios. For regional and teleseismic P waves recorded at the same station, the amplitude ratios of point sources are equivalent to their radiation pattern ratios, which is a function of take-off angle and azimuth, based on ray theory being implemented in a layered elastic media (Dahm, 1996).

On the other hand, the surface wave amplitude ratios are complex functions of the moment tensors and depths. When the source depth h is much less than the wavelength as in the case of nuclear tests, certain surface wave eigenfunction terms are reduced to 0,

$$l_2(h) = \mu \frac{dl_1}{dz}\bigg|_h = 0, \tag{6}$$

$$r_3(h) = \mu \left(\frac{dl_1}{dz} - kr_2\right)\bigg|_h = 0, \tag{7}$$

$$r_4(h) = 0, \tag{8}$$

where r and l are components of the Rayleigh and Love wave motion-stress vectors, and the excitation of Rayleigh and Love waves is given by

$$\boldsymbol{u}^{Rayl}(\boldsymbol{x},\omega) = \boldsymbol{G^R}[U_1 + U_2 cos2\phi + U_3 sin2\phi], \tag{9}$$

$$\boldsymbol{u}^{Love}(\boldsymbol{x},\omega) = \boldsymbol{G^L}[U_2 sin2\phi - U_3 cos2\phi], \tag{10}$$

where $\boldsymbol{G^R}$ and $\boldsymbol{G^L}$ are given by

$$\boldsymbol{G^R}(\boldsymbol{x}; h, \omega) = \sum_n \frac{k_n r_1(h)}{8cUI_1}\sqrt{\frac{2}{\pi k_n r}}\exp\left[i\left(k_n r + \frac{\pi}{4}\right)\right][r_1(z)\hat{\boldsymbol{r}} + ir_2(z)\hat{\boldsymbol{z}}], \tag{11}$$

$$\boldsymbol{G^L}(\boldsymbol{x}; h, \omega) = \sum_n \frac{ik_n l_1(h)}{8cUI_1}\sqrt{\frac{2}{\pi k_n r}}\exp\left[i\left(k_n r + \frac{\pi}{4}\right)\right] l_1(z)\hat{\boldsymbol{\phi}}, \tag{12}$$

in which μ is the shear modulus, *r* is the distance, *z* is the depth, $\hat{\boldsymbol{r}}, \hat{\boldsymbol{z}}, \boldsymbol{\phi}$ are the unit vectors for 3 cylindrical coordinates, and k_n is the nth root of the wave number (Aki and Richards, 2002). The radiation pattern coefficients U_1, U_2, U_3 are given by

$$U_1 = \frac{1}{2}\left(\boldsymbol{M}_{xx} + \boldsymbol{M}_{yy}\right) - \left(1 - \frac{2\beta^2}{\alpha^2}\right)\boldsymbol{M}_{zz}, \tag{13}$$

$$U_2 = \frac{1}{2}\left(\boldsymbol{M}_{xx} - \boldsymbol{M}_{yy}\right), \tag{14}$$

$$U_3 = \boldsymbol{M}_{xy}. \tag{15}$$

When two events E1 and E2 are both shallow and closely located, they share similar $\boldsymbol{G^R}$ and $\boldsymbol{G^L}$. Hence these terms can be canceled out by calculating the amplitude ratios. The analytical form of Rayleigh and Love wave amplitude ratios would be functions of moment tensors $\boldsymbol{M}_{E1}, \boldsymbol{M}_{E2}$, Vp/Vs ratios β/α, and station azimuth ϕ,

$$\boldsymbol{A^R}|_{\frac{E1}{E2}} = \frac{(U_1 + U_2cos2\phi + U_3sin2\phi)|_{E1}}{(U_1 + U_2cos2\phi + U_3sin2\phi)|_{E2}}, \tag{16}$$

$$\boldsymbol{A^L}|_{\frac{E1}{E2}} = \frac{(U_2sin2\phi - U_3cos2\phi)|_{E1}}{(U_2sin2\phi - U_3cos2\phi)|_{E2}}, \tag{17}$$

This means we can also take the path effects away by calculating amplitude ratios of surface waves.

For vertical component P waves, we cut 3-second time windows right after the hand-picked P arrivals, and cross-correlate to measure the amplitude ratios. We calculate two different terms,

$$A^1 = \frac{\int \boldsymbol{u}(\tau - t)\boldsymbol{v}(\tau)d\tau}{\int \boldsymbol{v}^2(\tau)d\tau} \tag{18}$$

$$A^2 = \frac{\int \boldsymbol{u}^2(\tau)d\tau}{\int \boldsymbol{u}(\tau - t)\boldsymbol{v}(\tau)d\tau} \tag{19}$$

where ***u(t)*** and ***v(t)*** are the wave segments of two events after cross-correlation. The terms A^1 and A^2 are similar to the waveform-coherency-based amplitude ratio defined in an adjoint tomographic inversion (Tao *et al.*, 2017) and reflect the waveform similarity of the cross correlations. The term A^1 generally represents $\boldsymbol{u}/\boldsymbol{v}$, while A^2 represents $1/(\boldsymbol{v}/\boldsymbol{u})$ after an appropriate time shift. If $\boldsymbol{u}$ and $\boldsymbol{v}$ have the same waveform shape (correlation coefficient =1), A^1 and A^2 would be identical and equal to the amplitude amplification factor (AAF) (Tan and Helmberger, 2007). Otherwise, A^1 will be smaller and A^2 will be larger than the AAF. Therefore, it's logical to take A^1 and A^2 as lower and upper bound to assess the waveform-coherency-dependent amplitude ratio variations. We take the natural logarithm of the absolute values of A^1 and A^2, and choose their mean as data and the half deviation as data uncertainty. Besides, we extract the polarity difference from cross correlations as part of the differential data. We use 1 and -1 to represent the same and opposite polarities of the event pair at each station, and use their difference (2) as 3 times standard deviation error (99% confidentce limit).

Measurement of the Rayleigh and Love wave amplitude ratios and errors is similar to that of body waves. We choose the time window to be 60s centered at the peak envelope amplitudes for cross correlations. Specifically for Rayleigh waves, we take the largest deviation between $ln(|A^1|)$ and $ln(|A^2|)$ for both radial and vertical components for the amplitude ratio errors.

2.3 Bayesian Markov Chain Monte Carlo inversion

We use the Metropolis-Hasting Markov Chain Monte-Carlo (MCMC) method to estimate the posterior probability density functions (PDFs) by fitting the differential measurements (i.e., amplitude ratios and polarity differences) of body and surface waves. The MCMC inversion follows a Bayesian framework, which produces model distribution from data fittings and the a priori information (Tarantola, 2005),

$$p(\boldsymbol{m}|\boldsymbol{d}) \propto p(\boldsymbol{m}) * l(\boldsymbol{d}|\boldsymbol{m}), \tag{18}$$

where the $p(\boldsymbol{m})$ and $p(\boldsymbol{m}|\boldsymbol{d})$ are prior and posterior PDFs, respectively. d indicates the amplitude ratio data, including logarithmic amplitude ratios and polarity differences. m represents the 6 independent source parameters (M_w, ζ, χ, strike, dip, and rake) for each event, in total 12 parameters for an event pair. Conversion from the data to model is performed through the likelihood function, which describes how the predictions from a model fit the data within data error. Our likelihood function is defined as the following equation,

$$l(\boldsymbol{d}|\boldsymbol{m}) = \frac{1}{\sqrt{(2\pi)^N |\boldsymbol{C_d}|}} exp\left(-\frac{1}{2}(G(\boldsymbol{m}) - \boldsymbol{d})^T \boldsymbol{C_d^{-1}}(G(\boldsymbol{m}) - \boldsymbol{d})\right), \tag{19}$$

where G is the forward simulation operator, and $\boldsymbol{C_d}$ is the data covariance matrix. We assume that $\boldsymbol{C_d}$ is diagonal:

$$\boldsymbol{C_d}_{ii} = \sigma_i^2, \qquad i \in [1, N] \tag{20}$$

$$\boldsymbol{C_d}_{(i+N)(i+N)} = \varepsilon_i^2, \qquad i \in [1, N] \tag{21}$$

where σ_i and ε_i are the standard deviation errors of logarithmic amplitude ratio and polarity difference at the i^{th} station, respectively. To avoid the inversion being dominated by data points of minimal errors, we set σ_i to be no less than 0.05, corresponding to ~5% amplitude ratio difference. Here we assumed no correlation between data errors for different stations, different phases, and various measurement types (amplitude ratios vs. polarities), which may not best reflect the true covariance. But because the P and surface waves are well separated, and Rayleigh and Love waves have orthogonal direction of vibration, their interferences are unlikely substantial. It's also reasonable to ignore the covariance between amplitude ratios and polarities, as they would be correlated only when the observation is close to the nodal, which is the minority of all stations.

We use Markov Chain Monte Carlo (MCMC) method to sample the posterior PDF $p(m|d)$. For low-dimension problems, brutal force algorithms are sufficient to sample the posterior PDF. When the dimensionality increases (e.g. >10), the volume of the model space increases exponentially, and the available trials become too sparse to grid-search the models. Instead, MCMC allows us to sample higher dimension distributions of known form but difficult to grid-search. Guided by the form of the posterior PDF, a Markov Chain randomly walks through the model space and results in an ensemble of models which density follows the target distribution. The models move to higher posterior probabilities with Gaussian random perturbations, and can still accept less likely models and thus jumping out of the local minimums (Hastings, 1970).

We generate 200 Markov Chains, and eventually keep 1/4 chains with highest posterior probability to avoid being trapped in low posterior minima. For each chain, we randomly generate 200 samples, and select the one of highest posterior probability as the initial draw. We apply the Gaussian proposal distributions to perturb the model at each step towards a new model. The Gaussian proposal distribution of each parameter has a standard deviation of 1/10 standard deviation of its prior distribution. We follow the Metropolis Hasting algorithm (Hastings, 1970) to drive the random walk, but different from conventional Metropolis-Hasting algorithm which perturb all parameters simultaneously, we propose new models by sampling one parameter while keeping the other parameters at their current values (Jia *et al.*, 2020a). The parameter being perturbed is randomly selected. This approach ensures a high acceptance rate and improves the efficiency of convergence. Our Markov Chains usually converge in hundreds to thousands of iterations, but we choose a conservative number of burn-in samples to be 20000. After the burn-in stage, we keep the next 20000 samples in each chain, and combine 50 chains to form the final ensemble for the posterior PDFs.

3 SYNTHETIC TEST

We first benchmarked diffMT with synthetics, using the configuration of two collocated nuclear tests at the North Korea test site. Nuclear events have shallow burial depths and short duration, thus fitting our assumptions well. We put the pair at a depth of 0.6 km, and with the E1 moment tensor as (M_w 4.53, $\boldsymbol{\Lambda}^{\boldsymbol{ISO}}$=86%, strike/dip/rake=70°/40°/70°) and the E2 moment tensor as (M_w 4.44, $\boldsymbol{\Lambda}^{\boldsymbol{ISO}}$=73%, strike/dip/rake=160°/30°/90°). Using these source parameters, we calculated synthetic seismograms for 8 regional (within epicentral distance of 15°) and 33 teleseismic (epicentral distance between 30° and 90°) stations (Fig. 2a). The velocity model used is based on a combination of a 3-layer 1D elastic model (Ford *et al.*, 2009) and the iasp91 model (Kennett *et al.*, 1995). We collected real seismic noise for the used stations, and added them to the synthetic waveforms (Fig. 2b) for a similar level of signal-to-noise ratio (SNR) as natural nuclear test events. After adding the noise, the synthetic surface waves still have high SNRs, while the body waves are generally hard to observe in broadband. This is similar to the real data for most North Korea nuclear tests.

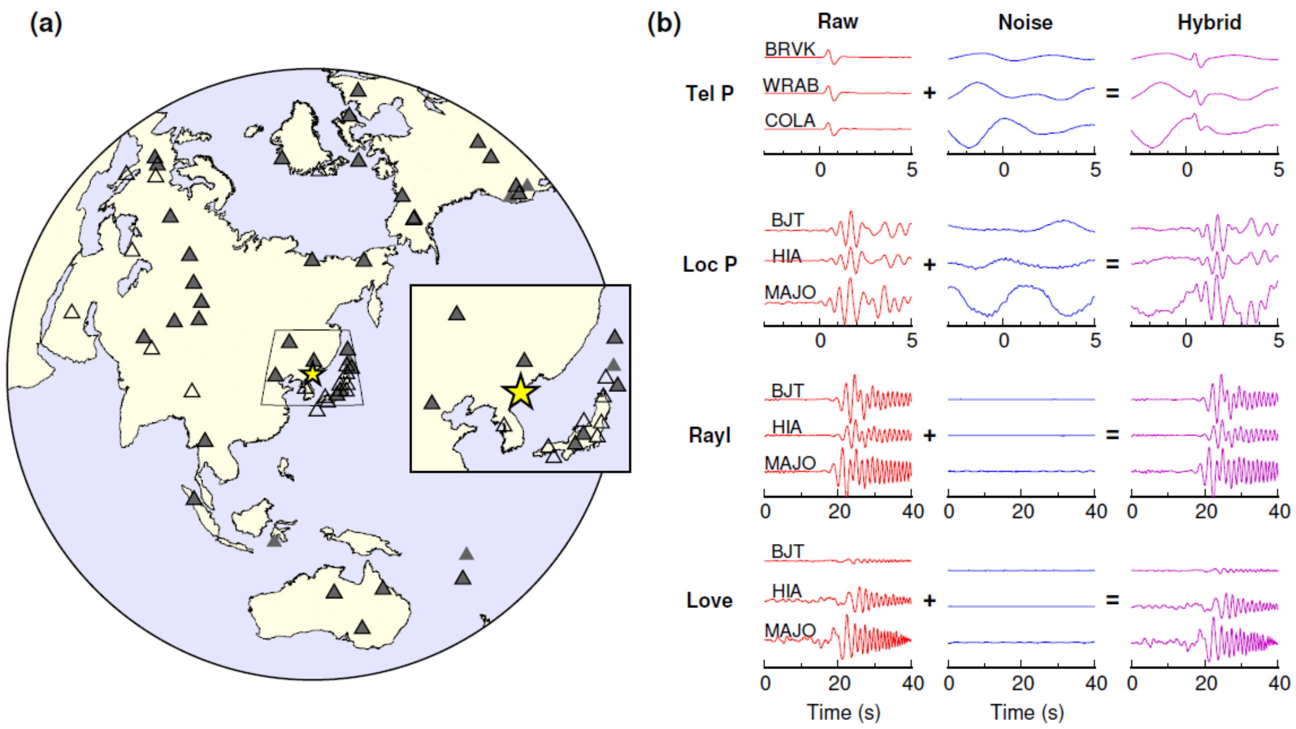

Figure 2. Generation of synthetic waveforms in our test. (A) Configuration of collocated sources (yellow star) and the seismic stations (gray triangles). Black-outlined triangles are the stations used in the following real-data inversions. The inset box shows the regional stations. (B) Adding real noise (blue lines) to the raw seismograms (red lines) for the hybrid synthetic data (purple lines).

We first applied the gCAP inversion on the two events. We filtered the data and synthetics between 0.03-0.1 Hz for regional surface waves and 0.5-1.0 Hz for teleseismic body waves. Modeling the real site amplifications of high frequency P waves is difficult, so we normalized the P waves data to the synthetic wave amplitudes and only fit the waveform shapes. We also fixed the source depths to 0.6 km, approximated from Voytan et al. (2019), due to the limited data resolution. The moment tensor results have ~60% isotropic components for both E1 and E2 (Fig. 3), which is smaller than the input model. Moreover, the double couple focal mechanisms deviate ~30 degrees from the input values.

We estimated the moment tensor standard deviation errors using 200 bootstrapping resamples, and observed substantial uncertainties for both E1 and E2 (Fig. S1). Given the minor data misfits (Fig. 3), the nontrivial moment tensor errors reflect poor data constraints due to limited frequency band and sparse network.

After obtaining the gCAP solutions and uncertainties, we converted them to Gaussian a priori information for the diffMT inversion. We measured the amplitude ratios of regional and teleseismic P waves, and regional Rayleigh and Love waves. We filtered the surface waves between 0.03-0.1 Hz, consistent with the gCAP inversion. For the P waves, we applied 0.5-2.0 Hz filter band for higher signal-to-noise ratios. Most waveforms of the two events show high similarity, with polarity flips for some surface wave components (Fig. 4a). The amplitude ratios show clear azimuthal variations (Fig. 4b), which are presumably caused by the radiation pattern difference of the two events.

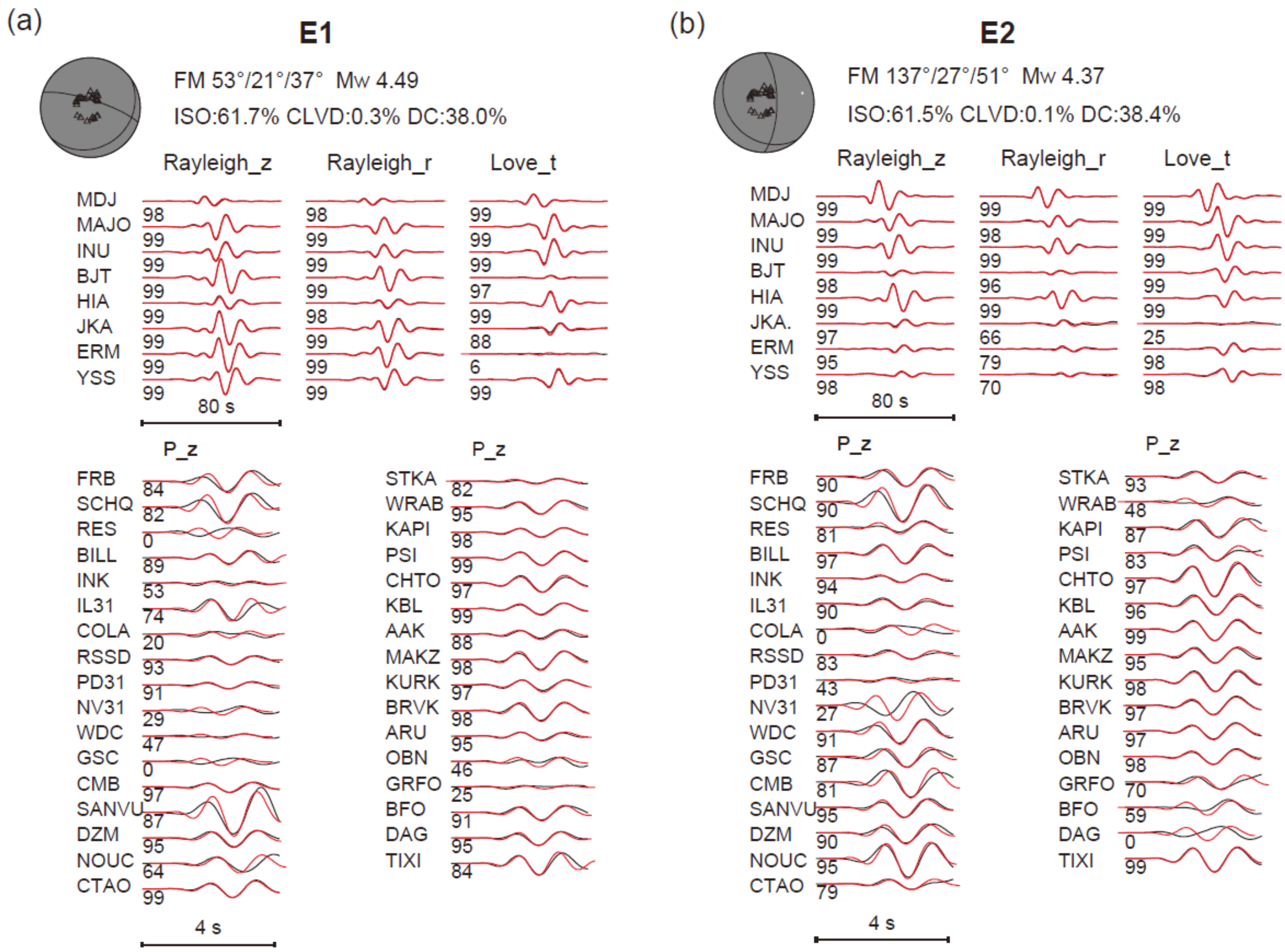

Figure 3. gCAP inversion results for the two synthetic events. The black and red lines indicate data and synthetic waveforms, respectively. The numbers leading the waveforms are the cross-correlation coefficients between data and synthetics.

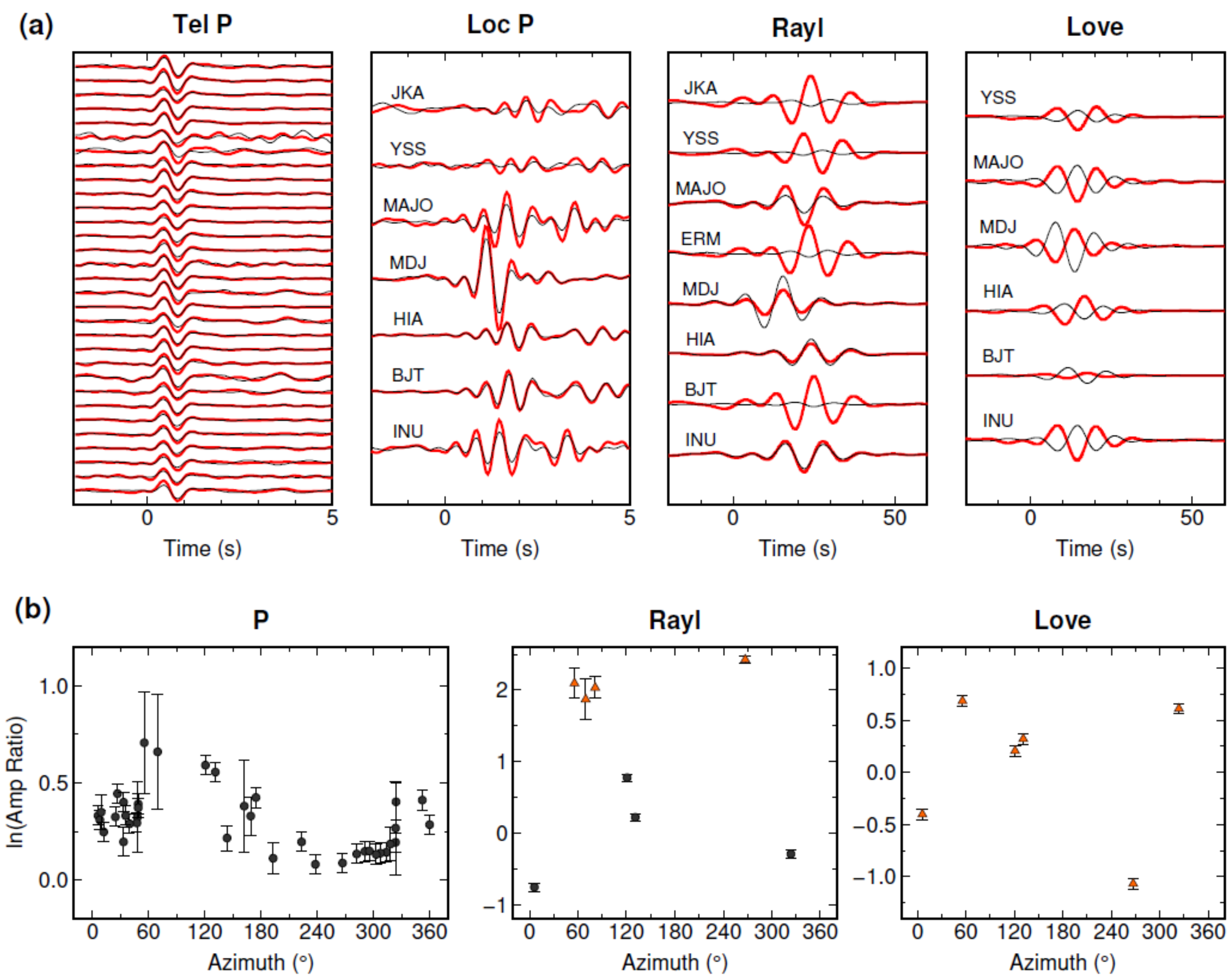

Figure 4. Measurement of amplitude ratios between two synthetic events. (A) Cross-correlated waveforms for teleseismic P (Tel P), regional P (Loc P), Rayleigh and Love waves, respectively. (B) Amplitude ratios for P, Rayleigh and Love waves as a function of the station azimuth. The Tel P and Loc P observations are plotted together. Black circles and orange triangles represent consistent and flipping polarities, respectively. The standard deviation errors are shown with the error bars.

With the amplitude ratio data derived from absolute amplitudes, we conducted diffMT inversion using MCMC sampling. The inversion results and data fittings are shown in Fig. 5. The posterior probability density functions (PDFs) are significantly narrower than the prior PDFs, showing reduced moment tensor uncertainties (Fig. 5a). The optimal source parameters from diffMT inversion are also closer to the true input values, and the moment magnitude difference is 0.08, closer to the true difference (0.09) than the prior difference (0.12) (Fig. 5b). The 3D rotation angle between diffMT (61°/51°/61°) and true solution of E1 is 13°, significantly less than the 27° rotation between the gCAP and true solution (Fig. 5c). Similar improvement is observed for E2, where the 3D rotation angle between diffMT (150°/26°/73°) and the true solution is 10°, less than the rotation angle between the gCAP and true solution (22°) (Fig. 5c). This is primarily because the azimuthal variations of the amplitude ratios, which is well fit by the diffMT synthetics (Fig. 5d), provide additional constraints that improve the moment tensor accuracy.

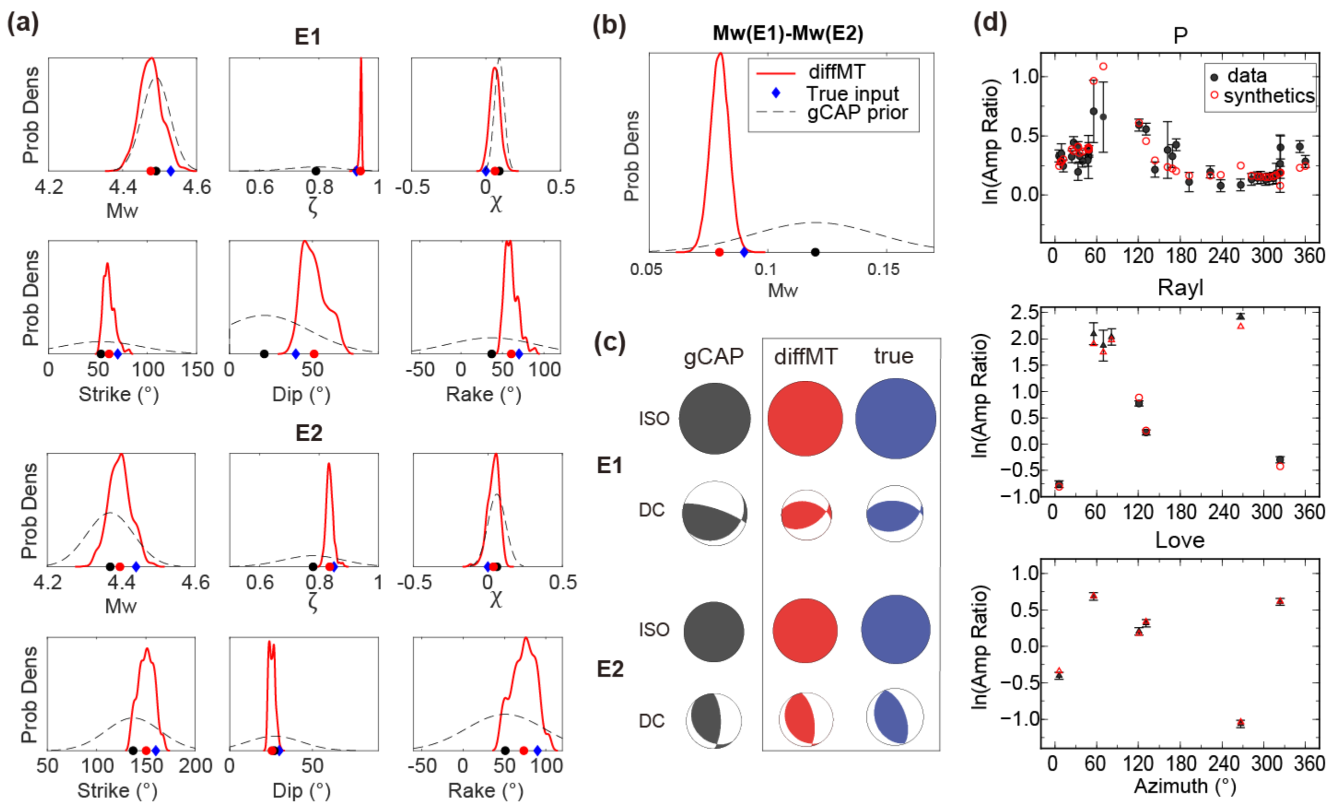

Figure 5. DiffMT inversion results for the two synthetic events. (a) The gCAP prior (dashed black lines) and the diffMT posterior (red lines) PDFs of the moment tensor solutions of the two events. The prior (gCAP) is

from Gaussian fitting of bootstrapping uncertainties. Black and red dots indicate the gCAP optimal solution and mean of the diffMT posterior distribution, respectively. Blue diamond represents the true input value. See legend in (b). (b) The prior (dashed black lines) and posterior (red lines) PDFs of the moment magnitude difference between E1 and E2. Symbols are similar to that in (a). (c) Comparison of the isotropic (DC) and double couple (DC) focal mechanisms for the gCAP (black) and diffMT (red) solutions. Blue beachballs show the true focal mechanisms. The sizes of beachballs are proportional to the corresponding magnitudes. (d) Amplitude ratio fittings for the diffMT solution. Black squares and red symbols show the amplitude ratio data and predictions from the moment tensor models, respectively. Circles and triangles represent consistent and flipping polarities, respectively.

4 APPLICATION ON NORTH KOREA NUCLEAR TESTS

We applied our diffMT algorithm to the three North Korea nuclear tests on Feb 2013, Jan 2016 and Sep 2016, respectively, by conducting inversions on three event pairs using seismograms from regional (within epicentral distance of 15°) and teleseismic (epicentral distance between 30° and 90°) stations (Fig. 3). The number of observations for all 3 events are not identical due to the varying station availability across the time period, but since the overlapping stations are the majority, the azimuthal and distance coverage differences are trivial. Similar to the synthetic test, we first run gCAP inversion using the regional surface waves in velocity filtered between 0.03-0.1 Hz, and the teleseismic P waves in velocity filtered between 0.5-1.0 Hz. The narrow P wave filter band is a compromise between signal observability and modeling capability. We fixed the depths to be 0.6 km, similar to the estimations from Voytan et al. (2019), to avoid depth ambiguities. The inversion results show that both the regional and teleseismic waveforms are fit well (Fig. 6). We observe 50~70%

isotropic component for these events, which is generally consistent with other moment tensor inversion studies (Cesca *et al.*, 2017, Chiang *et al.*, 2018, Ford *et al.*, 2009). The distributions of the moment tensors estimated from the bootstrapping resampling suggest that all the source parameter components have large uncertainties (Fig. S2). Particularly, the isotropic component fraction and double couple orientations are not well constrained. The wide range of model uncertainties makes it difficult to discriminate the explosions or to analyze the tectonic release mechanisms.

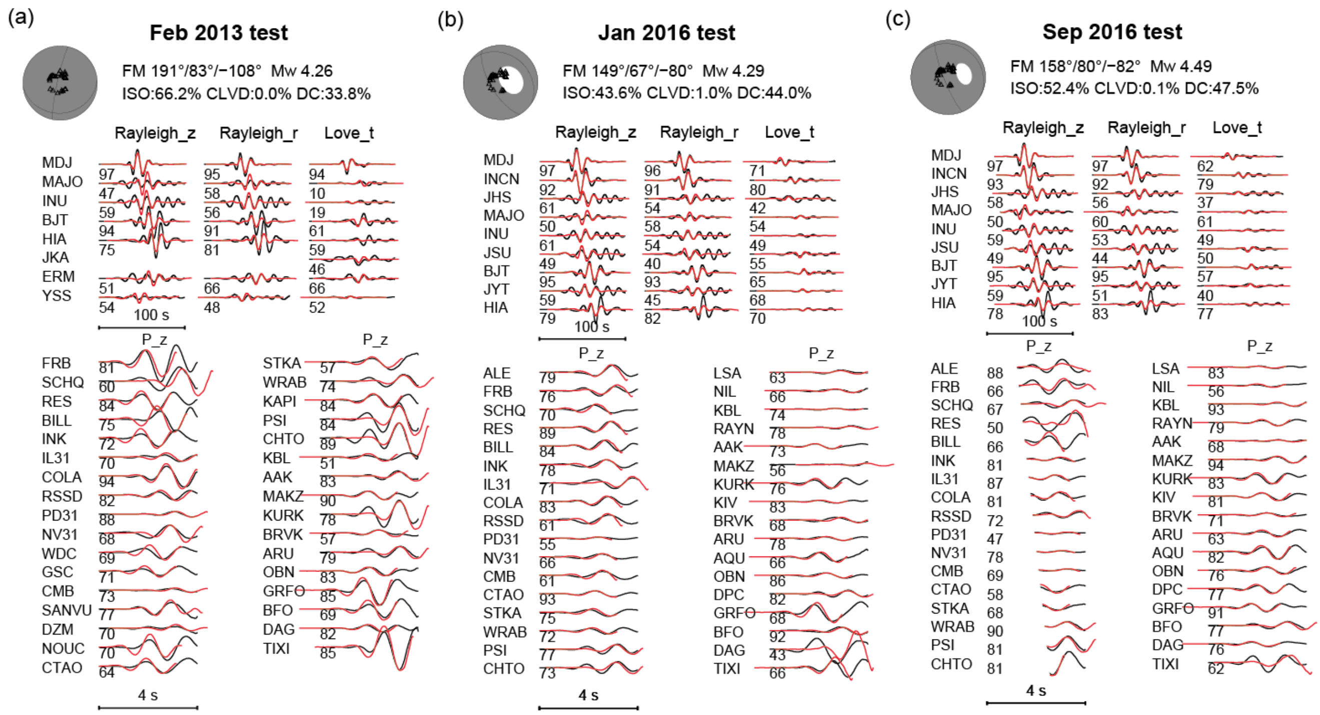

Figure 6. gCAP inversion results for the 3 studied North Korea nuclear explosions on (A) Feb 2013, (B) Jan 2016 and (C) Sep 2016, respectively. The symbols are similar to that in Fig. 3.

We measure amplitude ratios of the 3 event pairs among these three tests, using regional and teleseismic P waves between 0.5-2.0 Hz, and the Rayleigh and Love waves between 0.03-0.1 Hz. Waveforms of different events show high similarity, indicating robust measurements of the amplitude ratios (Fig. S3). The amplitude ratios have moderate azimuthal variation patterns (Fig. 7), which suggests different double-couple mechanisms under the dominant isotropic components.

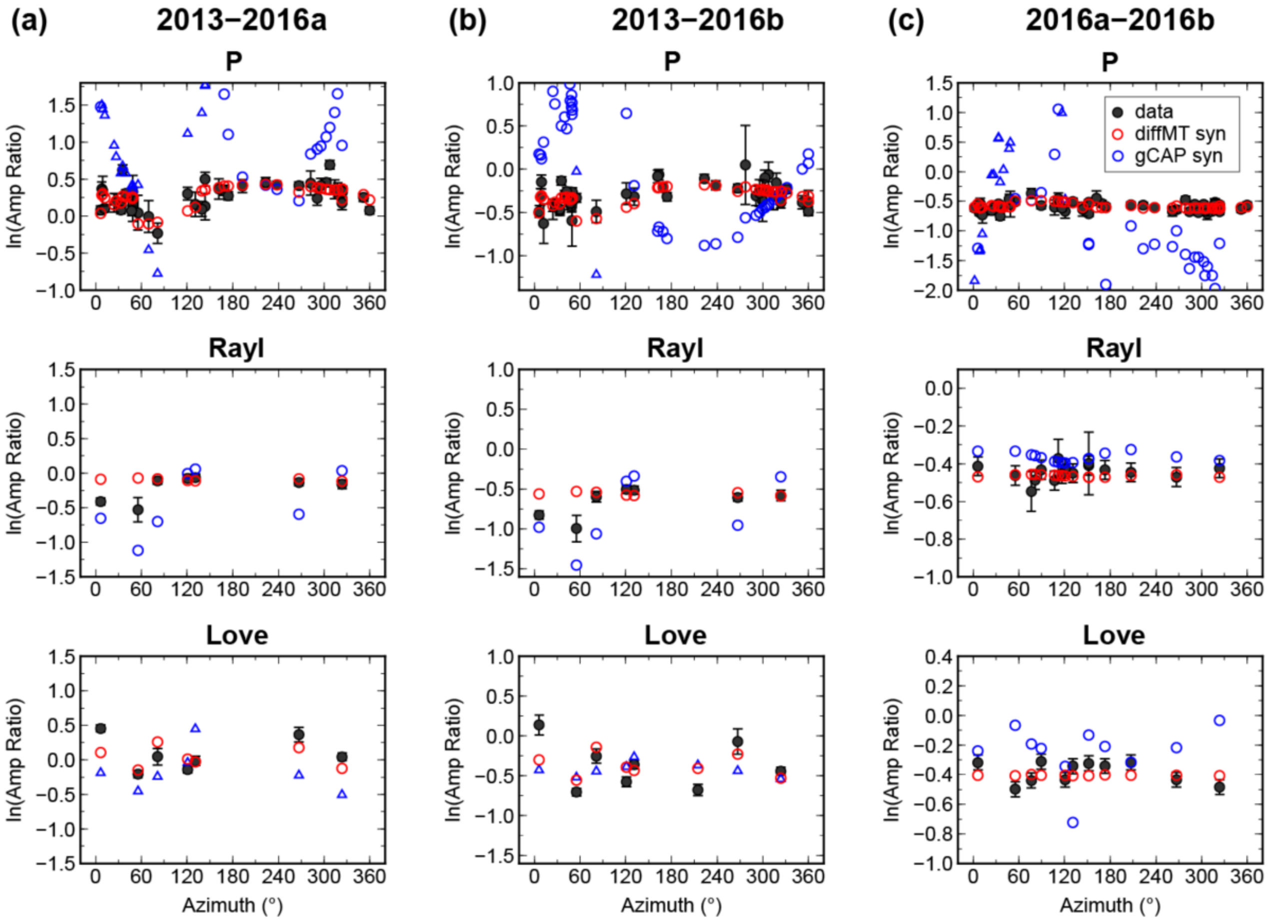

Figure 7. Amplitude ratios among the Feb 2013, Jan 2016 (2016a), and Sep 2016 (2016b) events. Three pairs are shown in (a)-(c), respectively. Circles and triangles represent consistent and flipping polarities, respectively. Black symbols with error bars show the amplitude ratio measurements. Blue and red symbols indicate the amplitude ratio predictions from the gCAP and diffMT solutions, respectively.

We further applied three separate diffMT inversions on these pairs. We did not choose doing one inversion for all events, due to the rapidly growing number of unknowns (N*6) for N events, which would pose a significant challenge to the nonlinear searching efficiency. Conducting multiple paired inversions would be the most applicable way of diffMT application on the real-world seismic event clusters. To avoid the inversion being trapped to pure isotropic sources (ζ=1) which generates very low Love wave amplitudes and numerically unstable ratios, we tapered the prior of ζ (equation 1) from its maximum bootstrapping value (0.98/0.96/0.96 for the Feb 2013, Jan 2016, and Sep 2016 events) to 1. The existence of Love waves also does not support pure isotropic source mechanisms. The diffMT posterior probability density functions (PDFs) are shown in Fig. 8. The posterior PDFs for each event are generally consistent from different pairs (Fig. 8a). Still, we can observe mismatches for some components, such as the rake angle for the Feb 2013 event, and CLVD parameter for the two 2016 tests (Fig. 8a). This is because models that fit amplitude ratio data for different pairs can have different biases from varying data errors. As long as they have overlapping model space, they do not contradict each other since the overlapped models could fit the data for both pairs. On the other hand, the CLVD factor χ may not be well constrained, because the CLVD component is a minor term accompanied with the DC mechanism (Zhu and Ben Zion, 2013), while the DC part is already second order compared to the dominant isotropic mechanism.

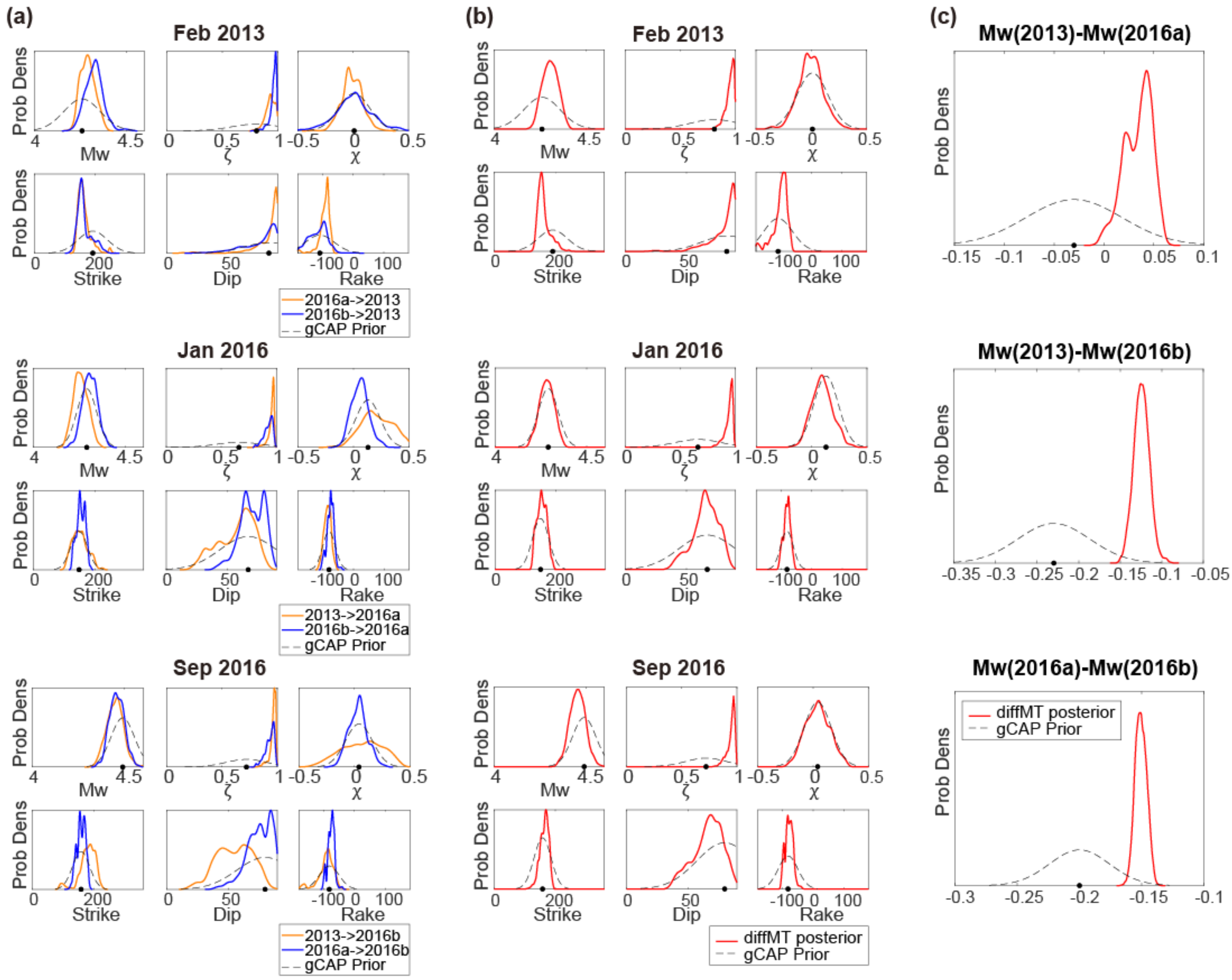

Figure 8. DiffMT inversion results for the event pair of the Feb 2013 and Jan 2016 tests. (a) The gCAP prior (dashed black lines) and the diffMT posterior (solid lines) PDFs of the moment tensor solutions of the two events. Solid lines in different colors indicate the posterior PDFs derived with different pairing events. Black dots show the optimal gCAP solution. (b) Combined posterior PDFs (solid red lines) plotted with the gCAP prior PDFs (dashed black lines). (c) The prior (dashed black lines) and posterior (red lines) PDFs of the moment magnitude differences.

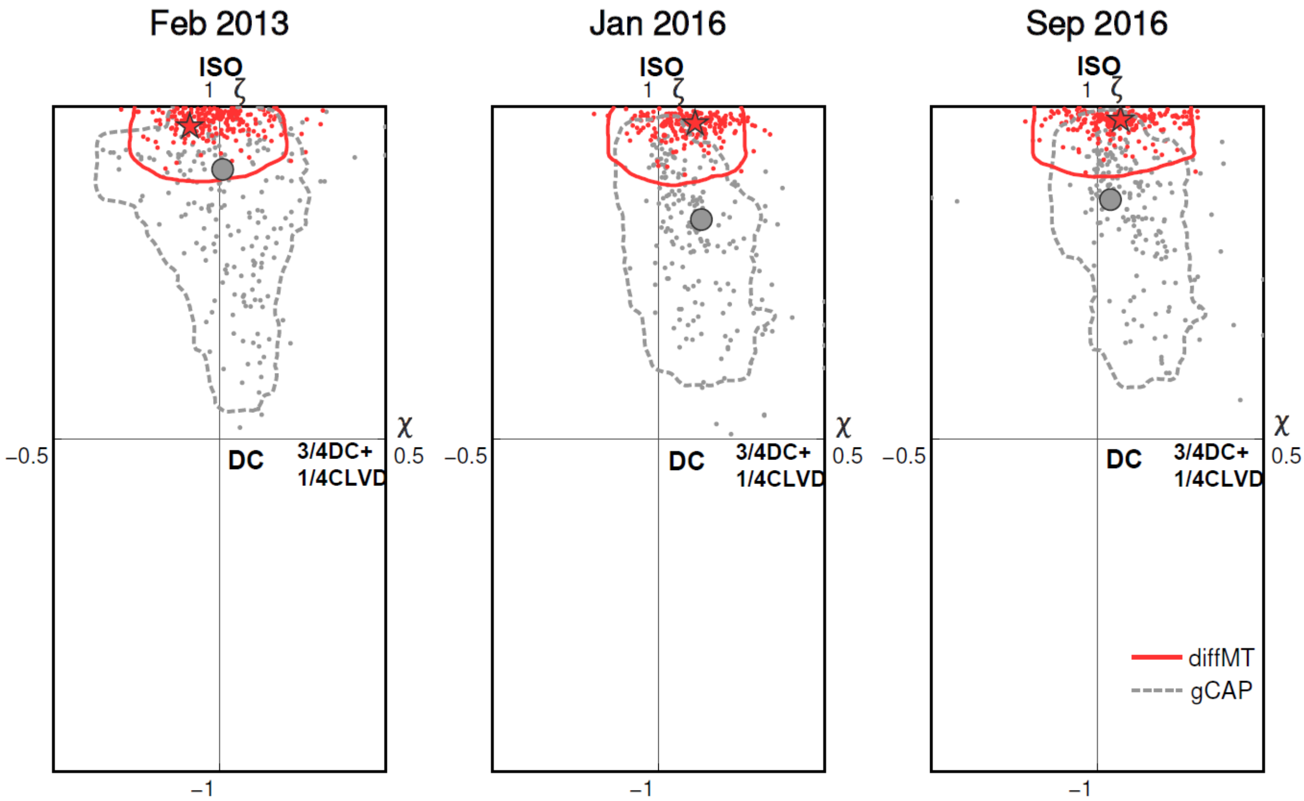

Figure 9. Prior (gCAP) and posterior (diffMT) distributions of ζ and χ for the three studied events. Red star and gray circle indicate diffMT and gCAP solution, respectively. The diffMT samples (red scattered dots) are contoured by the 90% confidence limit lines (red solid line), while the gray scattered dots and dashed lines are the gCAP samples and 90% confidence limits.

We multiplied the diffMT posterior PDFs of each event from different pairs for the overall posterior distributions (Fig. 8b). The posterior PDFs are significantly narrower than the prior PDFs, suggesting tighter constraints from the amplitude ratio measurements. In particular, the proportion of the isotropic components (ζ^2) are much better resolved and significantly more dominant (~90%) than the prior distributions (Fig. 9), which strongly suggest explosive source mechanisms. Meanwhile, diffMT inversions reduce the uncertainties of the moment magnitude differences (average standard deviation error of 0.04 for prior and 0.01 for posterior) (Fig. 8c), and make it much easier to compare the size of these nuclear tests. Therefore, the diffMT results could improve explosion discrimination and size comparison for the studied North Korea nuclear tests.

Moreover, diffMT inversion significantly reduces the uncertainty of the DC component (strike, dip, rake in Fig. 8b). To illustrate the improvement, we compared the double couple focal mechanism ensembles for the gCAP prior and diffMT posterior distributions (Fig. 10). The gCAP prior ensemble shows highly scattered strike and dip angles. In contrast, the diffMT focal mechanisms converge well, with strike and dip variances generally less than 40 degrees. The diffMT solutions suggest a similar high angle dip-slip as the tectonic release for the three nuclear tests.

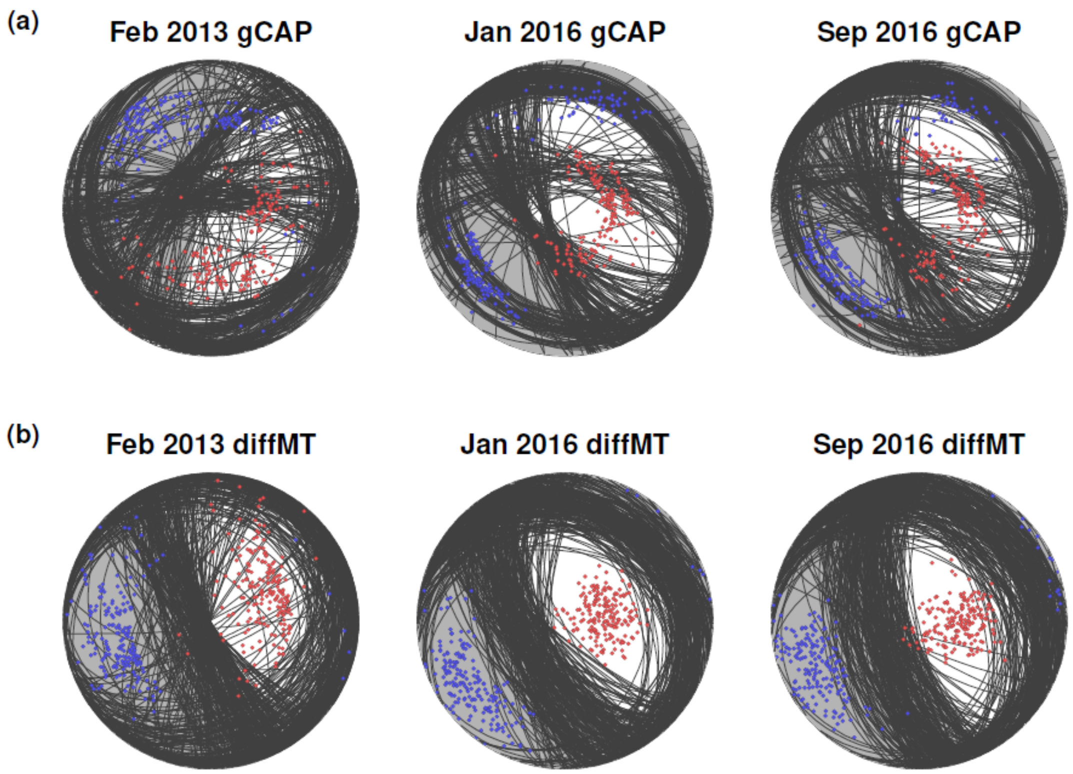

Figure 10. Scatter plot of the focal mechanisms from the (a) gCAP prior and (b) diffMT posterior ensembles. Red and blue dots are the P and T axes of the focal mechanisms, respectively.

5 DISCUSSION

Our application of the diffMT inversion on the North Korea nuclear tests shows better-resolved moment tensors. Although the gCAP inversion uses absolute body and surface wave amplitudes, it does not capture the patterns of amplitude ratios which provide extra constraints on moment tensors. The gCAP and diffMT solutions fit the regional and teleseismic waveforms almost equally well (Fig. S4), suggesting that the absolute amplitude information can hardly distinguish the two moment tensor solutions. In contrast, our final diffMT solution, which is sampled near the mean of the posterior distributions, fits amplitude ratios significantly better than the gCAP solution (Fig. 7). This is because the absolute amplitude information contains the unknown path and site effects that cause misfits that translates to model uncertainties assuming a simple velocity model. On the other hand, diffMT does not require highly accurate velocity models, thus finding better MT solutions from the gCAP ensembles.

Relative moment tensor inversions have been developed and implemented in various studies (Dahm, 1996, Plourde and Bostock, 2019, Voytan *et al.*, 2019, Xu *et al.*, 2020). Compared with these methods, our diffMT inversion uses a two-step approach to combine the waveforms with the amplitude ratio information, and quantify moment tensor uncertainties in a Bayesian framework, which provides a natural uncertainty analysis. Introducing the Bayesian framework also eliminates the need of choosing reference events, and avoids the magnitude trade-offs with constraints from the priors. Moreover, diffMT includes surface waves, making it suitable for events with sparse local observations. However, our method still introduces certain assumptions which may bring additional model errors. We did not consider depth phases in the P wave amplitude ratio modeling. Although the influence of 1D depth phases appears insignificant (Fig. S5), the impact of depth phase variations due to the 3D surface topographic reflections are moderate and need further investigations(Avants, 2014, Rodgers *et al.*, 2010). Besides, the calculations of body wave amplitude ratios rely on take-off angles calculated with a layered model, and the influence of the source side structural heterogeneities on the ray parameters is presumably low but not negligible. Overall, structural heterogeneities may still bias our inversion results, suggesting that full numerical wavefield simulations with more realistic earth models are needed in the future.

We summarized our final diffMT solutions in Table 1. The proportions of the isotropic components are all around 90% (Table 1), substantially more dominant than the gCAP estimates of around 50-70%, or some other solutions of 50%-60% for the North Korea nuclear tests (Vavryčuk and Kim, 2014, Cesca *et al.*, 2017, Ford *et al.*, 2009). Note that surface waves alone can not discriminate the isotropic and vertical-dipping CLVD sources, as their radiation patterns are similar around the edge of focal sphere. However, the P waves can cover the central portion of the beachball, and the strength of the azimuthal-varying P amplitude ratios constrains how much they deviate from uniform radiation (isotropic source). The moment magnitudes of these three events are 4.31, 4.28, 4.43, respectively, suggesting similar sizes for the Feb 2013 and Jan 2016 tests, followed by the larger Sep 2016 test. Double couple components are mostly dip-slip normal faulting events, and the steep dip angles of tectonic release are suggested by various studies in this region (Cesca *et al.*, 2017, Ford *et al.*, 2009, Barth, 2014). The DC orientations are also consistent with Cesca et al. (2017). But similar to the bottlenecks of most moment tensor inversion, our diffMT algorithm only resolve point source moment tensors for events with clear body and surface waves. Therefore, we skipped the 2009 North

Korea nuclear test in our study due to the low SNRs (Fig. S6). We also did not include the Sep 2017 test (M 6.3), because it likely involves sequential explosions, tectonic releases and collapses (Xu *et al.*, 2020), which introduces wave complexities (Fig. S6) beyond the point-source assumption. Further investigations of time-dependent source parameters are needed for large and complicated nuclear explosions.

The ISO/DC/CLVD decomposition used in this paper, while used extensively in nuclear monitoring (Ford *et al.*, 2009, Cesca *et al.*, 2017, Vavryčuk and Kim, 2014, Chiang *et al.*, 2018), is not the only physical interpretation. Following Aki&Richard's classical model, full moment tensor could be viewed as oblique opening of the fault for one of the two non-perpendicular planes (Aki and Richards, 2002, Tape and Tape, 2013). Also, a moment tensor can be decomposed as a crack tensor plus a double couple (CDC), in which the tensile crack direction is perpendicular to the fault plane of shear motion (Tape and Tape, 2013, Alvizuri and Tape, 2018). These various kinematic expressions of seismic source can lead to different understandings of the physical processes of nuclear tests.

In our current parameterization of the diffMT inversion, we assume Gaussian priors for the source parameters, which may not best represent the moment tensor variety in the parameter space, and encounter wrap-around at the boundaries. In practice, we truncated the Gaussian functions at the boundaries to avoid jumps for strike/dip/rake. Although moderate changes of prior shape won't significantly influence the diffMT inversion, there are better ways to avoid the non-uniformity of the source parameter distributions. For example, Tape and Tape (2013, 2015) formulate 5 uniformed parameters that can be mapped to an eigenvalue vector and a triple, to represent unique moment tensors. This way leads to even distributions of moment tensors in the parameter space, which could benefit the prior selection for the diffMT in the future.

Table 1. Moment tensor solutions for the 3 studied North Korea nuclear tests.

	M_w	ζ	χ	Strike	Dip	Rake	Λ^{ISO}(%)	Λ^{DC}(%)	Λ^{CLVD}(%)
Feb 2013 (prior)	$4.26^{+0.20}_{-0.20}$	$0.81^{+0.19}_{-0.44}$	$0.01^{+0.14}_{-0.14}$	191^{+96}_{-96}	83^{+7}_{-40}	-108^{+94}_{-72}	66^{+34}_{-50}	34^{+50}_{-34}	0^{+2}_{-0}
Feb 2013 (diffMT)	$\mathbf{4.31^{+0.06}_{-0.07}}$	$\mathbf{0.94^{+0.06}_{-0.07}}$	$\mathbf{-0.09^{+0.27}_{-0.1}}$	$\mathbf{154^{+51}_{-17}}$	$\mathbf{79^{+10}_{-22}}$	$\mathbf{-92^{+21}_{-58}}$	$\mathbf{88^{+12}_{-12}}$	$\mathbf{12^{+11}_{-11}}$	$\mathbf{0^{+1}_{-0}}$
Jan 2016 (prior)	$4.29^{+0.10}_{-0.10}$	$0.66^{+0.34}_{-0.40}$	$0.13^{+0.22}_{-0.22}$	149^{+53}_{-53}	67^{+23}_{-46}	-80^{+41}_{-41}	44^{+56}_{-37}	56^{+27}_{-43}	0^{+8}_{-0}
Jan 2016 (diffMT)	$\mathbf{4.28^{+0.07}_{-0.07}}$	$\mathbf{0.95^{+0.03}_{-0.09}}$	$\mathbf{0.11^{+0.15}_{-0.17}}$	$\mathbf{161^{+18}_{-33}}$	$\mathbf{61^{+20}_{-16}}$	$\mathbf{-90^{+28}_{-10}}$	$\mathbf{91^{+5}_{-17}}$	$\mathbf{9^{+17}_{-6}}$	$\mathbf{0^{+1}_{-0}}$
Sep 2016 (prior)	$4.49^{+0.13}_{-0.13}$	$0.72^{+0.28}_{-0.37}$	$0.04^{+0.24}_{-0.24}$	158^{+56}_{-56}	80^{+10}_{-46}	-82^{+64}_{-64}	52^{+48}_{-40}	48^{+40}_{-42}	0^{+6}_{-0}
Sep 2016 (diffMT)	$\mathbf{4.43^{+0.09}_{-0.05}}$	$\mathbf{0.96^{+0.03}_{-0.09}}$	$\mathbf{0.07^{+0.16}_{-0.21}}$	$\mathbf{163^{+21}_{-25}}$	$\mathbf{66^{+18}_{-23}}$	$\mathbf{-89^{+30}_{-10}}$	$\mathbf{92^{+6}_{-16}}$	$\mathbf{8^{+16}_{-6}}$	$\mathbf{0^{+1}_{-0}}$

6 CONCLUSIONS

We developed a differential moment tensor (DiffMT) inversion algorithm that resolves moment tensors of clustered seismic event pairs using relative measurements. It starts with a conventional moment tensor inversion for the a priori solutions, followed by inversion on amplitude ratio information for the refinements. Application of diffMT on three North Korea nuclear tests between 2013 and 2016 leads to reduced errors of isotropic components and double couple focal mechanisms. Their moment tensors have ~90% explosive components, which are more dominant compared with some conventional results of 50%~60%, providing opportunity for better explosion discrimination.

The associated tectonic release components are small but nontrivial high angle dip-slip mechanisms. The seismic moment differences between events are also better resolved, which could improve energy estimation of nuclear tests. With tighter constraints on the double couple focal mechanisms, we expect the diffMT method to be applied to various types of seismic events.

REFERENCES

Aki, K. & Richards, P.G., 2002. *Quantitative seismology,* edn, Vol., pp. Pages.

Alvizuri, C. & Tape, C., 2018. Full moment tensor analysis of nuclear explosions in North Korea, *Seismol. Res. Lett.,* 89, 2139-2151.

Avants, M., 2014. Effects of near-source heterogeneity on wave fields emanating from crustal sources observed at regional and teleseismic distances, UC Santa Cruz.

Bai, Q., Ni, S., Chu, R. & Jia, Z., 2020. gCAPjoint, A Software Package for Full Moment Tensor Inversion of Moderately Strong Earthquakes with Local and Teleseismic Waveforms, *Seismological Society of America,* 91, 3550-3562.

Ballard, S., Hipp, J.R., Begnaud, M.L., Young, C.J., Encarnacao, A.V., Chael, E.P. & Phillips, W.S., 2016. SALSA3D: A tomographic model of compressional wave slowness in the Earth's mantle for improved travel-time prediction and travel-time prediction uncertainty, *Bull. Seismol. Soc. Am.,* 106, 2900-2916.

Barth, A., 2014. Significant release of shear energy of the North Korean nuclear test on February 12, 2013, *JSeis,* 18, 605-615.

Bazargani, F., Hale, D. & Hayes, G.P., 2013. Tensor-Guided Fitting of Subducting Slab Depths, *Bull. Seismol. Soc. Am.,* 103, 2657-2669.

Bozdağ, E., Peter, D., Lefebvre, M., Komatitsch, D., Tromp, J., Hill, J., Podhorszki, N. & Pugmire, D., 2016. Global adjoint tomography: first-generation model, *Geophysical Journal International,* 207, 1739-1766.

Cesca, S., Heimann, S., Kriegerowski, M., Saul, J. & Dahm, T., 2017. Moment tensor inversion for nuclear explosions: What can we learn from the 6 January and 9 September 2016 nuclear tests, North Korea?, *Seismol. Res. Lett.,* 88, 300-310.

Chiang, A., Ichinose, G.A., Dreger, D.S., Ford, S.R., Matzel, E.M., Myers, S.C. & Walter, W., 2018. Moment Tensor Source-Type Analysis for the Democratic People's Republic of Korea–Declared Nuclear Explosions (2006–2017) and 3 September 2017 Collapse Event, *Seismol. Res. Lett.,* 89, 2152-2165.

Covellone, B.M. & Savage, B., 2012. A quantitative comparison between 1D and 3D source inversion methodologies: Application to the Middle East, *Bulletin of the Seismological Society of America,* 102, 2189-2199.

Dahm, T., 1996. Relative moment tensor inversion based on ray theory: theory and synthetic tests, *Geophysical Journal International,* 124, 245-257.

Dreger, D., 1994. Empirical Green's function study of the January 17, 1994 Northridge, California earthquake, *Geophys. Res. Lett.,* 21, 2633-2636.

Duputel, Z., Rivera, L., Kanamori, H. & Hayes, G., 2012. W phase source inversion for moderate to large earthquakes (1990–2010), *Geophys. J. Int.,* 189, 1125-1147.

Ekström, G., Nettles, M. & Dziewoński, A., 2012. The global CMT project 2004–2010: Centroid-moment tensors for 13,017 earthquakes, *Physics of the Earth and Planetary Interiors,* 200, 1-9.

Fichtner, A., Kennett, B.L., Igel, H. & Bunge, H.-P., 2009. Full seismic waveform tomography for upper-mantle structure in the Australasian region using adjoint methods, *Geophysical Journal International,* 179, 1703-1725.

Ford, S.R., Dreger, D.S. & Walter, W.R., 2009. Source analysis of the memorial day explosion, Kimchaek, North Korea, *Geophys. Res. Lett.,* 36.

Ford, S.R., Walter, W.R. & Dreger, D.S., 2012. Event discrimination using regional moment tensors with teleseismic-P constraints, *Bulletin of the Seismological Society of America,* 102, 867-872.

Frohlich, C. & Davis, S.D., 1999. How well constrained are well-constrained T, B, and P axes in moment tensor catalogs?, *Journal of Geophysical Research: Solid Earth,* 104**,** 4901-4910.

Hardebeck, J.L. & Hauksson, E., 2001. Crustal stress field in southern California and its implications for fault mechanics, *Journal of Geophysical Research: Solid Earth,* 106**,** 21859-21882.

Hastings, W.K., 1970. Monte Carlo sampling methods using Markov chains and their applications.

Hauksson, E., 1994. State of stress from focal mechanisms before and after the 1992 Landers earthquake sequence, *Bull. Seismol. Soc. Am.,* 84**,** 917-934.

Hayes, G.P., Wald, D.J. & Keranen, K., 2009. Advancing techniques to constrain the geometry of the seismic rupture plane on subduction interfaces a priori: Higher-order functional fits, *Geochem. Geophys. Geosyst.,* 10.

Jia, Z., Ni, S., Chu, R. & Zhan, Z., 2017. Joint inversion for earthquake depths using local waveforms and amplitude spectra of Rayleigh waves, *Pure and Applied Geophysics,* 174**,** 261-277.

Jia, Z., Shen, Z., Zhan, Z., Li, C., Peng, Z. & Gurnis, M., 2020a. The 2018 Fiji Mw 8.2 and 7.9 deep earthquakes: One doublet in two slabs, *Earth Planet. Sci. Lett.,* 531**,** 115997.

Jia, Z., Wang, X. & Zhan, Z., 2020b. Multifault Models of the 2019 Ridgecrest Sequence Highlight Complementary Slip and Fault Junction Instability, *Geophys. Res. Lett.,* 47**,** e2020GL089802.

Kanamori, H. & Rivera, L., 2008. Source inversion ofWphase: speeding up seismic tsunami warning, *Geophys. J. Int.,* 175**,** 222-238.

Kennett, B.L., Engdahl, E. & Buland, R., 1995. Constraints on seismic velocities in the Earth from traveltimes, *Geophysical Journal International,* 122**,** 108-124.

Kikuchi, M. & Kanamori, H., 1991. Inversion of complex body waves—III, *Bull. Seismol. Soc. Am.,* 81**,** 2335-2350.

Lay, T., Burdick, L. & Helmberger, D.V., 1984. Estimating the yields of the Amchitka tests by waveform intercorrelation, *Geophysical Journal International,* 78**,** 181-207.

Lee, E.J., Chen, P., Jordan, T.H., Maechling, P.B., Denolle, M.A. & Beroza, G.C., 2014. Full-3-D tomography for crustal structure in southern California based on the scattering-integral and the adjoint-wavefield methods, *Journal of Geophysical Research: Solid Earth,* 119**,** 6421-6451.

Liu, H., Gurnis, M., Leng, W., Jia, Z. & Zhan, Z., 2021. Tonga Slab Morphology and Stress Variations Controlled by a Relic Slab: Implications for Deep Earthquakes in the Tonga-Fiji Region, *Geophys. Res. Lett.,* 48**,** e2020GL091331.

Minson, S.E. & Dreger, D.S., 2008. Stable inversions for complete moment tensors, *Geophys. J. Int.,* 174**,** 585-592.

Ni, S., Helmberger, D. & Pitarka, A., 2010. Rapid source estimation from global calibrated paths, *Seismological Research Letters,* 81**,** 498-504.

Plourde, A.P. & Bostock, M.G., 2019. Relative moment tensors and deep Yakutat seismicity, *Geophysical Journal International,* 219**,** 1447-1462.

Rodgers, A.J., Petersson, N.A. & Sjogreen, B., 2010. Simulation of topographic effects on seismic waves from shallow explosions near the North Korean nuclear test site with emphasis on shear wave generation, *Journal of Geophysical Research: Solid Earth,* 115.

Savage, B., Morency, C., Covellone, B.M., Rodgers, A. & Tromp, J., 2014. Short-period, anelastic and anisotropic, waveform-based 3D Middle East model to improve nuclear explosion monitoringRHODE ISLAND UNIV KINGSTON KINGSTON United States.

Simmons, N.A., Myers, S.C., Johannesson, G. & Matzel, E., 2012. LLNL-G3Dv3: Global P wave tomography model for improved regional and teleseismic travel time prediction, *Journal of Geophysical Research:*

Solid Earth, 117.

Tan, Y. & Helmberger, D., 2007. A new method for determining small earthquake source parameters using short-period P waves, *Bull. Seismol. Soc. Am.,* 97, 1176-1195.

Tao, K., Grand, S.P. & Niu, F., 2017. Full-waveform inversion of triplicated data using a normalized-correlation-coefficient-based misfit function, *Geophys. J. Int.,* 210, 1517-1524.

Tape, C., Liu, Q., Maggi, A. & Tromp, J., 2009. Adjoint tomography of the southern California crust, *Science,* 325, 988-992.

Tape, W. & Tape, C., 2012. A geometric setting for moment tensors, *Geophysical Journal International,* 190, 476-498.

Tape, W. & Tape, C., 2013. The classical model for moment tensors, *Geophys. J. Int.,* 195, 1701-1720.

Tape, W. & Tape, C., 2015. A uniform parametrization of moment tensors, *Geophys. J. Int.,* 202, 2074-2081.

Tarantola, A., 2005. *Inverse problem theory and methods for model parameter estimation,* edn, Vol., pp. Pages, SIAM.

Vallée, M., 2007. Rupture properties of the giant Sumatra earthquake imaged by empirical Green's function analysis, *Bull. Seismol. Soc. Am.,* 97, S103-S114.

Vavryčuk, V. & Kim, S.G., 2014. Nonisotropic radiation of the 2013 North Korean nuclear explosion, *Geophys. Res. Lett.,* 41, 7048-7056.

Voytan, D.P., Lay, T., Chaves, E.J. & Ohman, J.T., 2019. Yield estimates for the six north Korean nuclear tests from teleseismic P wave modeling and intercorrelation of P and Pn recordings, *Journal of Geophysical Research: Solid Earth,* 124, 4916-4939.

Waldhauser, F. & Ellsworth, W.L., 2000. A double-difference earthquake location algorithm: Method and application to the northern Hayward fault, California, *Bull. Seismol. Soc. Am.,* 90, 1353-1368.

Wang, D. & Hutko, A.R., 2018. Relative relocations of the North Korean nuclear tests from 2006 to 2017 using the Hi-Net array in Japan, *Geophysical Research Letters,* 45, 7481-7487.

Wang, X. & Zhan, Z., 2020a. Moving from 1-D to 3-D velocity model: automated waveform-based earthquake moment tensor inversion in the Los Angeles region, *Geophysical Journal International,* 220, 218-234.

Wang, X. & Zhan, Z., 2020b. Seismotectonics and Fault Geometries of the 2019 Ridgecrest Sequence: Insight From Aftershock Moment Tensor Catalog Using 3-D Green's Functions, *Journal of Geophysical Research: Solid Earth,* 125, e2020JB019577.

Xu, H., Ni, S., Liu, W., Zhu, H. & Wang, X., 2020. Focal mechanisms of the 2017 North Korean nuclear test and its early collapse event, *Geophys. J. Int.,* 220, 737-752.

Yang, T., Gurnis, M. & Zhan, Z., 2017. Trench motion-controlled slab morphology and stress variations: Implications for the isolated 2015 Bonin Islands deep earthquake, *Geophys. Res. Lett.,* 44, 6641-6650.

Zhan, Z., Helmberger, D., Simons, M., Kanamori, H., Wu, W., Cubas, N., Duputel, Z., Chu, R., Tsai, V.C. & Avouac, J.-P., 2012. Anomalously steep dips of earthquakes in the 2011 Tohoku-Oki source region and possible explanations, *Earth Planet. Sci. Lett.,* 353, 121-133.

Zhang, M. & Wen, L., 2013. High-precision location and yield of North Korea's 2013 nuclear test, *Geophysical Research Letters,* 40, 2941-2946.

Zhang, M. & Wen, L., 2015. Seismological evidence for a low-yield nuclear test on 12 May 2010 in North Korea, *Seismological Research Letters,* 86, 138-145.

Zhao, L.S. & Helmberger, D.V., 1994. Source estimation from broad-band regional seismograms, *Bulletin of the Seismological Society of America,* 84, 91-104.

Zhu, L. & Ben-Zion, Y., 2013. Parametrization of general seismic potency and moment tensors for source inversion of seismic waveform data, *Geophysical Journal International,* 194**,** 839-843.

Zhu, L. & Helmberger, D.V., 1996. Advancement in source estimation techniques using broadband regional seismograms, *Bulletin of the Seismological Society of America,* 86**,** 1634-1641.

Zhu, L. & Rivera, L.A., 2002. A note on the dynamic and static displacements from a point source in multilayered media, *Geophys. J. Int.,* 148**,** 619-627.

ACKNOWLEDGMENTS

Z. J. and Z. Z. thank and commemorate Don Helmberger for his advising and assistance. We thank the Global Seismic Network (GSN), the International Federation of Digital Seismograph Networks (FDSN), the French Global Network (G), and the Japan Meteorological Agency Seismic Network (JP) for collecting the seismic data, and thank the Incorporated Research Institutions for Seismology (IRIS) for providing public access to them. We thank editor Carl Tape, assistant editor Fern Storey, reviewer Alexandre Plourde, and two other anonymous reviewers for their valuable comments. We thank Jack Muir for helpful discussions. This work is supported by Air Force Research Laboratory (AFRL) Grant FA9453-18-C-0058.

DATA AVAILABILITY STATEMENT

All the data used in our study can be downloaded from the IRIS Data Management Center (http://ds.iris.edu/wilber3/find_event).